Selective Area Growth of Well-Ordered ZnO Nanowire Arrays with Controllable Polarity

Vincent Consonni,[†,¥,*] Eirini Sarigiannidou,[†,¥] Estelle Appert,[†,¥] Amandine Bocheux,[‡] Sophie Guillemin,[†,¥] Fabrice Donatini,[§,¶] Ivan-Christophe Robin,[‡] Joseph Kioseoglou,[⊥] and Florence Robaut[||]

[†]Univ. Grenoble Alpes, LMGP, F-38000 Grenoble, France, [¥]CNRS, LMGP, F-38000 Grenoble, France, [‡]CEA, LETI, MINATEC Campus, F-38054 Grenoble, France, [§]Univ. Grenoble Alpes, Inst NEEL, F-38042 Grenoble, France, [¶]CNRS, Inst NEEL, F-38042 Grenoble, France, [⊥]Physics Department, Aristotle University of Thessaloniki, 54124 Thessaloniki, Greece, and [||]Consortium des Moyens Technologiques Communs, Grenoble INP, 1260 rue de la Piscine, 38402 Saint-Martin d'Hères, France

ABSTRACT Controlling the polarity of ZnO nanowires in addition to the uniformity of their structural morphology in terms of position, vertical alignment, length, diameter, and period is still a technological and fundamental challenge for real-world device integration. In order to tackle this issue, we specifically combine the selective area growth on prepatterned polar *c*-plane ZnO single crystals using electron-beam lithography, with the chemical bath deposition. The
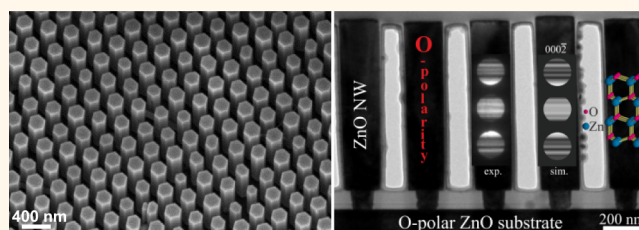
formation of ZnO nanowires with a highly controlled structural morphology and a high optical quality is demonstrated over large surface areas on both polar *c*-plane ZnO single crystals. Importantly, the polarity of ZnO nanowires can be switched from O- to Zn-polar, depending on the polarity of prepatterned ZnO single crystals. This indicates that no fundamental limitations prevent ZnO nanowires from being O- or Zn-polar. In contrast to their catalyst-free growth by vapor-phase deposition techniques, the possibility to control the polarity of ZnO nanowires grown in solution is remarkable, further showing the strong interest in the chemical bath deposition and hydrothermal techniques. The single O- and Zn-polar ZnO nanowires additionally exhibit distinctive cathodoluminescence spectra. To a broader extent, these findings open the way to the ultimate fabrication of well-organized heterostructures made from ZnO nanowires, which can act as building blocks in a large number of electronic, optoelectronic, and photovoltaic devices.

KEYWORDS: ZnO nanowires · polarity · selective area growth · chemical bath deposition · cathodoluminescence

Semiconductor nanowires (NWs) offer a large number of remarkable physical and chemical properties owing to their high aspect ratio at nanoscale dimensions.[1] They have received increasing basic and technological interest in the past decade and may act as building blocks in a wide variety of electronic, optoelectronic, and photovoltaic devices.[1−3] Among III−V and II−VI compound semiconductors, ZnO as abundant and nontoxic material may play a significant role in the next generation of these devices due to its wide band gap energy of 3.3 eV, its high exciton binding energy of 60 meV, its high electron mobility, and its large piezoelectric coefficient.[4,5] Its form of NWs can further be grown by a large number of surface scalable physical and chemical deposition techniques[4,5] such as thermal evaporation,[6] vapor-phase transport (VPT),[7] pulsed-laser deposition (PLD),[8]

standard and metal−organic chemical vapor deposition (MOCVD),[9,10] electrodeposition,[11] or chemical bath deposition (CBD).[12] Among them, the low-temperature and low-cost CBD technique is of particular interest and can be implemented quite easily on any type of substrate. However, the use of ZnO NWs in electronic, optoelectronic, and photovoltaic devices requires the precise control of the uniformity of their structural morphology (*i.e.*, position, vertical alignment, length, diameter, period) as well as of their polarity over large surface areas. The polarity control of wurtzite compound semiconductors such as ZnO is especially critical for mastering their surface configuration, reactivity, and stability as well as their electro-optical properties.[13] Until now, these requirements for ZnO NWs are still technological and fundamental challenges for real-world device integration.

In order to control their structural uniformity, the selective growth has been used to form ZnO NWs over predefined localized surface areas, although one single NW does not nucleate per hole.[14−24] More recently, the density and position of sparse ZnO NWs have been controlled by thermal evaporation or CBD *via* the selective area growth (SAG) using prepatterned substrates.[25−35] The substrates have been patterned through the use of an organic (*i.e.*, poly(methyl methacrylate) for instance) selective mask opened by submicrometer sphere lithography,[25] electron-beam lithography (EBL),[26−30,32] laser interference lithography,[31] or nanoimprint lithography.[33−35] Defect-controlled GaN micropatterns has also been employed for the SAG of ZnO NWs by MOCVD.[36] Nevertheless, in contrast to the SAG of sparse ZnO NW arrays that is relevant for electronic devices, the specific SAG of highly dense ZnO NW arrays is crucial for optoelectronic and photovoltaic devices.

The polarity of ZnO NWs has been a matter of debate over the past decade for all of the deposition techniques including the mask-free growth and SAG.[17,20,23,37−50] In the wurtzite crystalline structure of ZnO, negatively charged O planes are alternately stacked with positively charged Zn planes along the $\langle 0001 \rangle$ axis (*i.e.*, *c*-axis). By definition, the *c*-planes are polar, and the directions [0001] and [000$\bar{1}$] should be distinguished owing to the absence of center of inversion. When the vector starts with a Zn (respectively O) atom, points to an O (respectively Zn) atom, and is aligned along the + (respectively −) *c*-axis, the *c*-plane is by convention Zn- (respectively O-) polar. ZnO NWs have widely been reported to be Zn-polar, regardless of the vapor-phase or solution deposition techniques such as physical vapor deposition,[38,41,42,50] MOCVD,[44,45] or CBD.[39,40,46] Only recently, the growth of O-polar ZnO NWs by CBD has, however, been reported on O-polar *c*-plane ZnO single crystals.[47] Similarly, Sallet *et al.* have shown the growth of O-polar ZnO NWs by catalyst-assisted MOCVD on ZnO or sapphire substrates.[49] Additionally, the polarity of ZnO substrate strongly affects the structural morphology of ZnO nanostructures.[23,24,37,44,45,47,48] Concerning the growth of ZnO NWs by vapor-phase deposition techniques, it has initially been stated that ZnO NWs can only form on Zn-polar *c*-plane ZnO surfaces by chemical vapor transport and condensation using periodically polarity-inverted ZnO substrates[23,24] and thermal evaporation of oxide powders.[37] In contrast, the growth of ZnO NWs and nanowalls has subsequently been shown by PLD on O- and Zn-polar *c*-plane ZnO surfaces, respectively,[48] which appears to contradict the results of the two previous vapor-phase deposition techniques.[23,24,37] Also, Perillat-Merceroz *et al.* have shown by MOCVD that the formation of Zn-polar ZnO NWs is inevitably induced on O-polar *c*-plane ZnO surfaces *via* the nucleation of inversion domain boundaries (IDBs).[44,45] This may suggest that

ZnO NWs cannot grow with the O-polarity. With regard to the growth of ZnO NWs in solution by CBD, a thin polycrystalline seed layer of several tens of nanometers is initially deposited by dip- or spin-coating and consists of ZnO nanoparticles (NPs) preferentially oriented along the polar *c*-axis. Basically, the structural properties of ZnO NWs such as their position, vertical alignment, length, diameter, and period are strongly dependent upon the structural morphology of the ZnO seed layer.[47,51−56] It has been reported that only polar *c*-plane ZnO surfaces are highly reactive chemically and favor the formation of ZnO nanostructures by CBD.[47,56] In contrast, non polar *a*- and *m*-plane ZnO surfaces can instead induce the formation of 2D layers.[47] Overall, the results reported for the growth of ZnO NWs are strongly dependent upon the vapor-phase and solution deposition techniques used; in particular, it is still controversial whether ZnO NWs can form on both O- and Zn-polar ZnO surfaces as well as can have O- and Zn-polarity.

In this article, we address the issue of ZnO NW structural uniformity and polarity by combining SAG, using prepatterned polar *c*-plane ZnO single crystals by EBL, with CBD. The formation of highly dense ZnO NW arrays is shown, and their position, vertical alignment, dimensions, and polarity can precisely be controlled over large surface areas. It is found that no fundamental limitations prevent ZnO NWs from being O- or Zn-polar, and a general growth mechanism is gained for the SAG in solution. The high optical quality of O- and Zn-polar ZnO NWs is also examined. The findings described hereafter pave the way to the ultimate fabrication by design of ZnO NW-based electronic, optoelectronic, and photovoltaic devices.

RESULTS AND DISCUSSION

In order to thoroughly control the uniformity of the crystal orientation and polarity of the nucleation surface, bulk *c*-plane ZnO single crystals with either O- or Zn-polarity were used as substrates. These single crystals were initially patterned by EBL and reactive ion etching (RIE). A SiO_x/Si_xN_y double thin layer was deposited as selective mask by plasma-enhanced CVD instead of the usual organic mask used for the SAG of ZnO NWs.[25−35] The hole diameter and period can therefore be controlled over a wide range of dimensions from 50 nm to 1 μm: here, the hole diameters of 107 ± 4 and 178 ± 7 nm were used on O- and Zn-polar *c*-plane ZnO single crystals, respectively, while their period was 330 nm, as revealed in Figures 1a and 2a. The patterned single crystals were subsequently drowned in a chemical precursor solution mixed in deionized water, which was composed of zinc nitrate and hexamethylenetetramine (HMTA) in an equimolar ratio and heated at moderate temperature.[12,51]

The structural morphology of ZnO NWs grown by CBD on patterned O- and Zn-polar *c*-plane ZnO single crystals and under identical growth conditions is
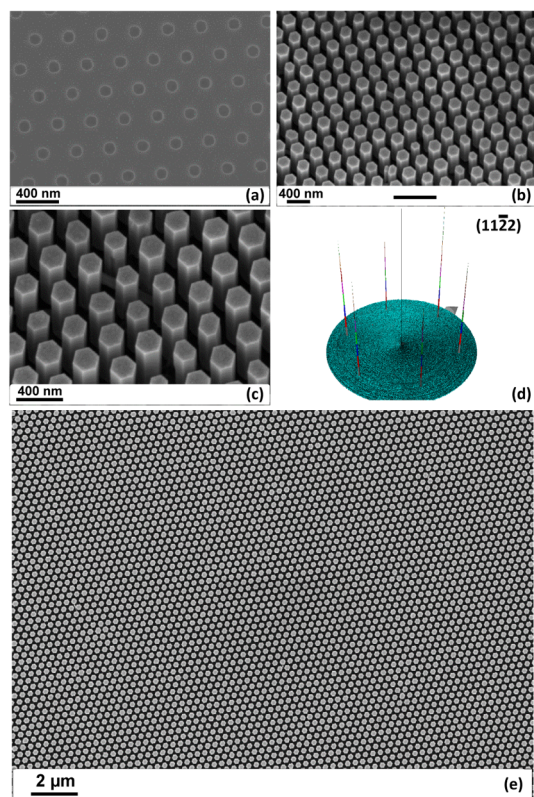
Figure 1. (a) Top-view FESEM image of patterned O-polar *c*-plane ZnO single crystals. (b,c) Tilted-view FESEM images of ZnO NWs grown by CBD on patterned O-polar *c*-plane ZnO single crystals. (d) Corresponding X-ray pole figures recorded on the (11$\bar{2}$2) asymmetric diffraction peak of ZnO NWs. (e) Low-magnification top-view FESEM image of ZnO NWs grown by CBD on patterned O-polar *c*-plane ZnO single crystals.

presented in Figures 1–4. Well-ordered and vertically aligned ZnO NWs are grown after 2.5 h as shown in the field-emission scanning electron microscopy (FESEM) images of Figures 1b,c,e and 2b,c as well as on the conventional transmission electron microscopy (TEM) images taken along the $\langle 10\bar{1}0 \rangle$ zone axis of Figures 3a and 4a. ZnO NWs present an aspect ratio of about 4.8 on O-polar *c*-plane ZnO single crystals, corresponding to a mean diameter and length of about 191 and 910 nm, respectively. In contrast, ZnO NWs exhibit a smaller aspect ratio of about 2.7 on Zn-polar *c*-plane ZnO single crystals with a mean diameter and length of about 216 and 577 nm, respectively. The distributions of ZnO NW diameter and length are narrow: the standard deviation of NW diameter and length on O- (respectively Zn-) polar *c*-plane ZnO single crystals is smaller than 12 (respectively 7) and 70 (respectively 10) nm, respectively, as deduced from TEM image analysis on more than 20 NWs. This indicates that the patterning of *c*-plane ZnO single crystals by EBL and RIE can control the position and typical dimensions of ZnO NWs through the mask width and height. Interestingly, no ZnO layer is formed on top of the Si$_x$N$_y$ mask, revealing that the mask can efficiently annihilate the

ZnO nucleation, as shown in Figures 3a and 4a. However, ZnO NWs typically spread on the mask while coming out of the hole. Interestingly, they expand radially to a greater extent on the mask when they are grown on O-polar *c*-plane ZnO single crystals, as shown in the TEM images of Figures 3a and 4a. When ZnO NWs come out of the mask, their diameter is increased by 78 and 20% on O- and Zn-polar *c*-plane ZnO single crystals, respectively. This is due to the radial growth of ZnO NWs along their vertical sidewalls. Accordingly, the final aspect ratio of ZnO NWs is almost doubled on O-polar *c*-plane ZnO single crystals in comparison with their growth on Zn-polar *c*-plane ZnO single crystals. This emphasizes that the axial and radial growth rates of ZnO NWs are in the present case larger on the O-polar *c*-plane ZnO single crystal than on the Zn-polar *c*-plane ZnO single crystal. This is, however, likely due to the difference in the mask width since no differences in the radial and axial growth rates were determined in the mask-free growth of ZnO by CBD on both O- and Zn-polar *c*-plane ZnO single crystals.[47] The vertical alignment of ZnO NWs is also optimal with a tilt angle smaller than 2° with respect to the normal to the substrate surface, as determined from the full width at half-maximum (fwhm) of X-ray pole figures recorded on the (0002) diffraction peak. This is much smaller than the tilt angle of ZnO NWs grown on top of ZnO NPs, even when the seed layer is highly textured along the *c*-axis.[56] Furthermore, the *m*-plane vertical sidewalls of ZnO NWs are parallel to each other as shown in Figures 1b,c and 2b,c, revealing the occurrence of a strong in-plane orientation. A homoepitaxial relationship is further revealed between ZnO NWs and *c*-plane ZnO single crystals by the X-ray pole figures recorded on the (11$\bar{2}$2) asymmetric diffraction peak in Figures 1d and 2d. The strong in-plane orientation and vertical alignment of ZnO NWs are highly desirable for the fabrication of core–shell heterostructures for solar
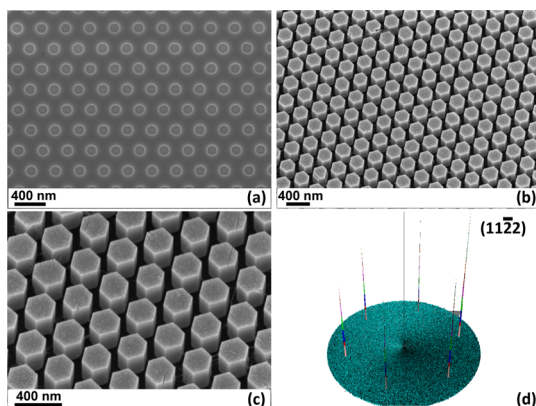

Figure 2. (a) Top-view FESEM image of patterned Zn-polar *c*-plane ZnO single crystals. (b,c) Tilted-view FESEM images of ZnO NWs grown by CBD on patterned Zn-polar *c*-plane ZnO single crystals. (d) Corresponding X-ray pole figures recorded on the (11$\bar{2}$2) asymmetric diffraction peak of ZnO NWs.
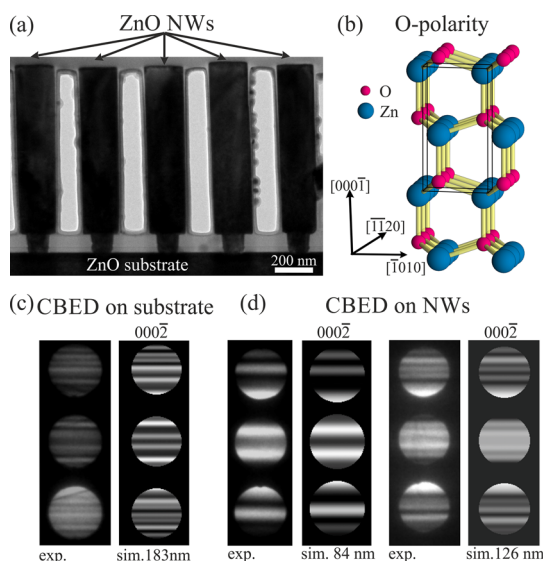
Figure 3. (a) Low-magnification cross-section conventional TEM image taken along the $\langle 10\bar{1}0 \rangle$ zone axis of ZnO NWs grown by CBD on patterned O-polar *c*-plane ZnO single crystals. (b) Atomistic view along the $\langle 11\bar{2}0 \rangle$ direction of O-polar *c*-plane ZnO with the wurtzite crystalline structure. The O-polar *c*-plane surface of ZnO is arbitrarily represented as O-terminated. (c) Experimental and simulated CBED patterns taken along the $\langle 10\bar{1}0 \rangle$ zone axis for thickness of 183 nm, revealing that *c*-plane ZnO single crystals are O-polar. (d) Experimental and simulated CBED patterns taken along the $\langle 10\bar{1}0 \rangle$ zone axis for both thickness of 84 and 126 nm, showing that ZnO NWs are O-polar. The central disk is the transmitted electron beam.

cells, in which shadowing effects are expected to play a significant role in the growth of the absorbing shell by PVD.[57] It should be noted that the uniformity of the structural morphology of ZnO NW arrays can be controlled over large surface areas as shown in the FESEM image of Figure 1e. The SAG of highly dense ZnO NW arrays by CBD with the same structural quality can therefore be achieved on both patterned O- and Zn-polar *c*-plane ZnO single crystals.

A general growth mechanism for the SAG of ZnO NWs in solution can be deduced on patterned polar *c*-plane ZnO single crystals. The solution temperature and the concentration of the chemical precursors are key parameters for the growth of ZnO NWs by CBD. These chemical precursors are zinc nitrate and HMTA here. Upon heating, Zn^{2+} ions are produced by zinc nitrate, while formaldehyde and ammonia are formed *via* the decomposition of HMTA as a heterocyclic organic compound.[12,58−61] OH^- ions are then produced *via* the chemical reaction of ammonia with water.[58−61] HMTA thus acts as a weak base and as a pH buffer, which slowly hydrolyzes and gradually produces OH^- ions, with the hydrolysis rate decreasing by increasing the pH.[58,59,62] The crystallization of ZnO is expected to be direct according to $Zn^{2+} + 2OH^- \leftrightarrow ZnO_s + H_2O$, but the formation of Zn intermediate hydroxide phases may occur.[58−62] Other sets of chemical reactions involve more complex Zn(II) species in

solution.[58−62] The main distinctions of the SAG of ZnO NWs by CBD when compared with the SAG by vapor-phase deposition techniques come from the presence of active ions in solution and from the negligible diffusion process at the surface. Basically, the significant electrostatic interactions of active OH^- and Zn^{2+} ions in solution occur with the charged polar *c*-planes within the holes of patterned ZnO single crystals. This is highly favorable for the nucleation of one single ZnO NW per hole. In contrast, the electrostatic interactions of active OH^- and Zn^{2+} ions with the Si_xN_y mask that is basically amorphous are much weaker. To some extent, the nucleation of ZnO on top of the mask is thus hampered. This is nevertheless dependent upon the hole period: for larger hole period, the homogeneous nucleation of ZnO in solution as well as the parasitic formation of ZnO on the mask can be detrimental. The SAG mechanisms of ZnO NWs accordingly follow two successive steps. Initially, the holes are preferentially filled with ZnO owing to strong electrostatic interactions with the active ions in solution and govern the diameter of ZnO NWs. Subsequently, ZnO NWs with nonpolar *m*-plane sidewalls can grow axially along the *c*-axis direction but also radially, spreading on the Si_xN_y mask. The elongation of ZnO NWs is governed by the mass transport of chemical precursors in solution, which is in principle activated thermally by the solution temperature and driven by the concentration of the
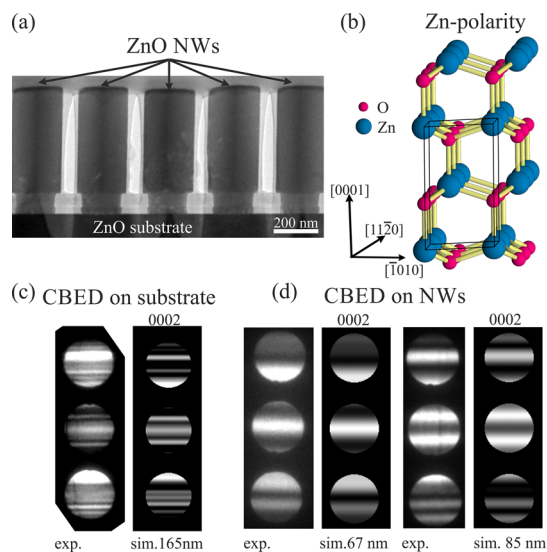

Figure 4. (a) Low-magnification cross-section conventional TEM image taken along the $\langle 10\bar{1}0 \rangle$ zone axis of ZnO NWs grown by CBD on patterned Zn-polar *c*-plane ZnO single crystals. (b) Atomistic view along the $\langle 11\bar{2}0 \rangle$ direction of Zn-polar *c*-plane ZnO with the wurtzite crystalline structure. The Zn-polar *c*-plane surface of ZnO is arbitrarily represented as Zn-terminated. (c) Experimental and simulated CBED patterns taken along the $\langle 10\bar{1}0 \rangle$ zone axis for thickness of 165 nm, revealing that *c*-plane ZnO single crystals are Zn-polar. (d) Experimental and simulated CBED patterns taken along the $\langle 10\bar{1}0 \rangle$ zone axis for both thickness of 67 and 85 nm, showing that ZnO NWs are Zn-polar. The central disk is the transmitted electron beam.

chemical precursors.[56,63] Also, the preferential shape of ZnO NWs by CBD can be retained outside the mask region. From thermodynamic considerations, surface energy anisotropy can result in the elongation of ZnO NWs by developing nonpolar *m*-plane sidewalls with low surface energy.[64] From kinetic considerations, the Zn^{2+} and OH^- active ions preferentially interact with the polar *c*-planes of the NW top facet, increasing the axial growth rate at the expense of the radial growth rate. The growth rate anisotropy is therefore favorable for retaining the preferential shape of ZnO NWs. Additionally, HMTA may also act as a capping agent on the nonpolar *m*-plane sidewalls,[65] but this hypothesis has not been confirmed by *in situ* attenuated total reflection Fourier transform infrared spectroscopy.[61]

In order to further investigate the structural morphology and growth mechanisms of ZnO NWs as well as to determine their polarity, high-resolution TEM imaging as well as convergent beam electron diffraction (CBED) measurements are presented in Figures 3–6. By convention in the wurtzite crystalline structure, it is well-known that the O-polarity corresponds to the growth along the $[000\bar{1}]$ direction where the $[000\bar{1}]$ axis is considered as parallel to the O–Zn bonding, as depicted in Figure 3b. In contrast, the $[0001]$ axis is considered as parallel to the Zn–O bonding; hence, the growth along the $[0001]$ axis is defined as the Zn-polarity, as presented in Figure 4b. The CBED technique is based on constructive and destructive interferences involving more than two diffracted electron beams.[66−68] A contrast difference in the intensity distribution basically occurs within the 0002 and $000\bar{2}$ diffracted discs of the CBED patterns, hence distinguishing between the O- and Zn-polarity of ZnO. The contrast difference depends both on the zone axis and crystal thickness as well as on the materials involved. It is well-established that the polarity of semiconductors with the wurtzite crystalline structure can reliably be characterized with the CBED patterns when collected along the $\langle 10\bar{1}0 \rangle$ zone axis for a crystal thickness larger than 50 nm.[66−68] However, the CBED technique does not provide any information about surface terminations, which should be distinguished from polarity. The O- and Zn-polarity of bulk *c*-plane ZnO single crystals is revealed in Figures 3c and 4c and was cross-checked by chemical wet etching using a HCl bath with a 2 mM concentration: the formation of pits and conjugated pits clearly occurs on O- and Zn-polar *c*-plane ZnO single crystals, respectively, which is in agreement with the polarity deduced from CBED measurements. Multiple experimental and simulated CBED patterns with EMS software using Block's wave method[69] were collected on different crystal thickness (*i.e.*, smaller and larger than 100 nm) in order to unambiguously determine the polarity of ZnO NWs. The contrast difference of the 0002 and $000\bar{2}$ diffracted discs is clearly revealed along the $\langle 10\bar{1}0 \rangle$
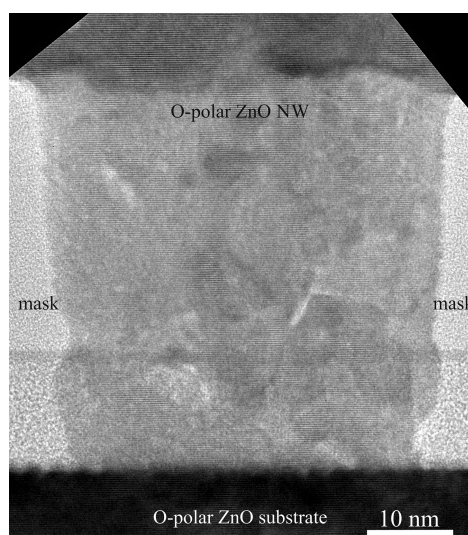

Figure 5. HRTEM image taken along the $\langle 11\bar{2}0 \rangle$ zone axis, revealing the interface between the O-polar ZnO NW and O-polar *c*-plane ZnO single crystal, the region of the ZnO NW grown inside the double mask, and the interface between the ZnO NW grown inside and outside the hole delimited by the mask. No sign for the presence of extended defects such as stacking faults, dislocations, twins, or IDBs is shown.

zone axis in Figures 3d and 4d as well as the agreement between the experimental and simulated CBED patterns. Importantly, ZnO NWs are found O-polar when grown on O-polar *c*-plane ZnO single crystals while they are Zn-polar when grown on Zn-polar *c*-plane ZnO single crystals. Consequently, ZnO NWs retain the O- or Zn-polarity of *c*-plane ZnO single crystals.

In order to support the aforementioned finding, extensive HRTEM images were recorded along the $\langle 11\bar{2}0 \rangle$ zone axis, especially on the interface area in between ZnO single crystals and NWs as well as along the growth of ZnO NWs in and outside the mask region. In Figures 5 and 6, a characteristic HRTEM image is presented where the wurtzite crystalline structure is clearly undisturbed. If a basal IDB had grown at the interface area or along the growth of ZnO NWs, a characteristic defect would have been identified in the HRTEM images: a basal IDB contains Zn–Zn and/or O–O bonds, and hence it should disturb the ...ABABAB... stacking sequence of the wurtzite crystalline structure. In contrast, the HRTEM images in Figures 5 and 6 clearly reveal that ZnO NWs are free of any extended defects such as stacking faults, twins, dislocations, or IDBs both at the interface area and inside or outside the mask region. As a consequence, the structural quality of ZnO NWs is high as no extended defects are formed in their center, neither at their bottom in the mask region nor at their top. The formation of IDBs can be excluded for the SAG of ZnO NWs in solution. The O- and Zn-polarity of *c*-plane ZnO single crystals is transferred unchanged to ZnO NWs grown by CBD.

The possibility to control the polarity of ZnO NWs grown in solution by SAG in addition to their position
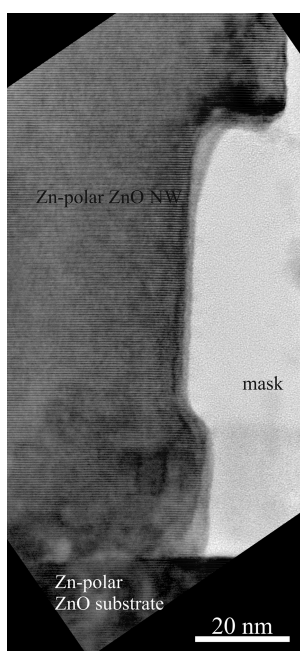
Figure 6. HRTEM image taken along the $\langle 11\bar{2}0 \rangle$ zone axis, showing the interface between the Zn-polar ZnO NW and Zn-polar *c*-plane ZnO single crystal, the region of the ZnO NW grown inside the double mask, and the interface between the ZnO NW grown inside and outside the hole delimited by the mask. No sign for the presence of extended defects such as stacking faults, dislocations, twins, or IDBs is revealed.

and structural uniformity (*i.e.*, length, diameter, period) is remarkable. This should be distinguished from the growth of ZnO NWs by vapor-phase deposition techniques, in which Zn-polar ZnO NWs are usually formed instead of O-polar ZnO NWs.[38,41,42,44,45,50] Perillat-Merceroz *et al.* have notably reported that Zn-polar ZnO NWs inevitably form spontaneously by MOCVD, even on O-polar *c*-plane ZnO surfaces.[44,45] The polarity of ZnO NWs can be reversed with respect to the O-polar *c*-plane ZnO nucleation surfaces owing to the formation of IDBs.[45] The same open questions arise from the self-induced growth of GaN NWs by MOCVD[70] or by molecular beam epitaxy, as well, in which sparse N-polar GaN NWs are nucleated on the Al-polar AlN buffer layer through the formation of IDBs.[71] The occurrence of IDBs in both ZnO and GaN NWs grown by vapor-phase deposition techniques has been attributed to strong Al or Si surfactant effects, respectively.[45,71] In contrast, these surfactant effects cannot take place for the growth of ZnO NWs in solution, which prevents IDBs from being formed. Therefore, the polarity control of ZnO NWs grown by SAG can be achieved when grown in solution by CBD and, importantly, no fundamental limitations prevent ZnO NWs from being O- or Zn-polar.

The 5 K cathodoluminescence (CL) spectra of O- and Zn-polar ZnO NWs are presented in Figure 7. The CL measurements were collected under low acceleration voltage and small spot size (*i.e.*, less than 10 nm), such

that the CL signal only originates from single ZnO NWs. Interestingly, O- and Zn-polar ZnO NWs exhibit distinctive optical properties. The CL spectra are governed by a large number of radiative transitions involving donor-bound excitons (DX_A)[72,73] in the range of 3.357 to 3.367 eV for both O- and Zn-polar ZnO NWs. The intensity of the near band edge (NBE) is about 2 to almost 3 orders of magnitude larger than the intensity of the broad defect emission band centered around 2.0 eV for O- and Zn-polar ZnO NWs, respectively. These show the high crystalline and optical quality of both O- and Zn-polar ZnO NWs. More importantly, in addition to the distinct intensity ratios that can directly be correlated with the CL measurements on ZnO single crystals,[74] the NBE of O-polar ZnO NWs is much more structured than the NBE of Zn-polar ZnO NWs. In O-polar ZnO NWs, the longitudinal and transversal free A-exciton states (FX_A) are resolved at 3.377 and 3.376 eV, respectively. Ionized donor-bound excitons also clearly occur at about 3.366 eV.[73] The NBE is further dominated by the intense doublet at 3.3619 and 3.3627 eV. These may be associated with the X_1 line that has exclusively been revealed in O-polar ZnO epilayers[75] and neutral donor-bound excitons *via* the I_4 (H) line, respectively.[72] The two-electron satellites (TES) related to the I_4 line arise at about 3.332 eV.[72] A broad shoulder also takes place at 3.358 eV and is assigned to neutral donor-bound excitons. Al, Ga, and In donors are expected to be involved here. In contrast, in Zn-polar ZnO NWs, the NBE is mainly governed by the dominant line at 3.3616 eV, which may be associated with neutral donor-bound excitons *via* the I_5 line.[72] A shoulder also occurs at 3.366 eV and is due to ionized donor-bound excitons.[73] TES are also expected in the shoulder lying in the range of 3.32 to 3.33 eV. The observed differences in the CL spectra of O- and Zn-polar ZnO NWs can directly be correlated with the distinct photoluminescence properties in O- and Zn-polar ZnO epilayers and single crystals.[74,75] The incorporation of impurities both in terms of concentration and nature may thus depend on the polarity of ZnO NWs. In particular, the more structured NBE may indicate that O-polar ZnO NWs incorporate more different impurities in nature than Zn-polar ZnO NWs, similarly to O-polar ZnO epilayers.[75] Additionally, the first and second longitudinal (LO) phonon replica of free A-excitons lie at 3.311 and 3.236 eV, respectively, and their intensity is more marked in O-polar ZnO NWs. In contrast, the first and second LO phonon replica of neutral donor-bound excitons arise at 3.292 and 3.218 eV, respectively, and their intensity is more pronounced in Zn-polar ZnO NWs.

The control of the structural uniformity and polarity of ZnO NWs opens the way to their efficient integration in electronic, optoelectronic, and photovoltaic devices. The need for assembling ZnO NW arrays with a pure single polarity is essential for piezoelectric nanogenerators,
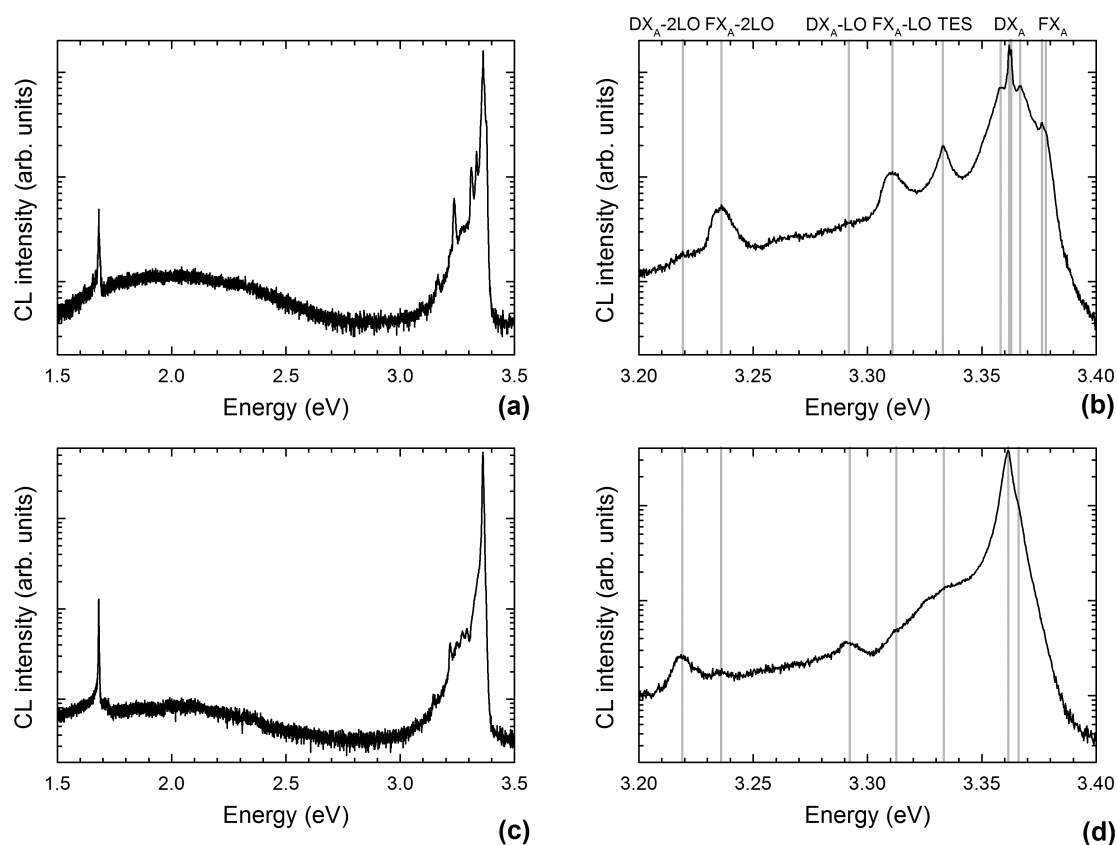
Figure 7. Five K CL spectra with a 600 grooves/mm grating of single (a) O- and (c) Zn-polar ZnO NWs. Five K CL spectra with a 1800 grooves/mm grating of single (b) O- and (d) Zn-polar ZnO NWs, emphasizing the NBE region. The CL spectra are collected under 5 kV acceleration voltage and spot size less than 10 nm at the center of single O- and Zn-polar ZnO NWs. The narrow lines in the range of 1.6 to 1.7 eV correspond to the second order of the NBE emission band.

in which the piezoelectric potential field along the polar *c*-axis is created under elastic deformation.[76] Furthermore, the fabrication of ZnO NW heterostructure arrays with a high structural uniformity is also critical for light-emitting diodes and photovoltaic devices,[77−79] where the optical extraction efficiency and absorption are strongly affected by the structural dimensions for instance.

CONCLUSION

In summary, we demonstrate, over large surface areas, the formation of highly dense epitaxial ZnO NW arrays with high structural uniformity and controllable polarity by combining SAG, using patterned *c*-plane ZnO single crystals by EBL and RIE, with CBD. A general growth mechanism is gained for the SAG of ZnO NWs in solution. These ZnO NWs are free of any

extended defects in their center and further exhibit high optical quality. Their polarity can be switched from O- to Zn-polar, depending on the polarity of patterned *c*-plane ZnO single crystals. The possibility to control the polarity of ZnO NWs grown in solution is remarkable and should be distinguished from their growth by vapor-phase deposition techniques. As a consequence, no fundamental limitations prevent ZnO NWs from being O- or Zn-polar, especially when grown in solution. The single O- and Zn-polar ZnO NWs also exhibit distinctive CL spectra. These findings open the way to the ultimate fabrication by design of ZnO NW arrays involving heterostructures or not with high interface and optical quality, great structural uniformity, and controllable polarity, which are the key conditions for their efficient integration in NW-based electronic, optoelectronic, and photovoltaic devices.

METHODS

Preparation and Patterning of ZnO Bulk Single Crystals. ZnO bulk single crystals from Crystec with O-polar $(000\bar{1})$ and Zn-polar (0001) crystal orientations were used as substrates. Prior to any patterning process, their surface was prepared chemically by chemical−mechanical polishing and thermal heat treatment under oxygen atmosphere. A silicon dioxide SiO_x layer with a

thickness of 30 nm was initially formed by plasma-enhanced CVD. Subsequently, a silicon nitride Si_xN_y layer acting as a selective mask was deposited with a thickness of 60 nm by plasma-enhanced CVD. The position of the holes in the mask were eventually defined and opened by EBL followed by RIE.

Fabrication of ZnO NWs by CBD. ZnO NWs were grown under identical conditions by CBD on top of prepatterned polar *c*-plane ZnO single crystals kept in a stove heated up to 90 °C. The

solution of chemical precursors consisted of mixing in deionized water zinc nitrate hexahydrate ($Zn(NO_3)_2 \cdot 6H_2O$) and hexamethylenetetramine ($C_6H_{12}N_4$) from Sigma-Aldrich in the equimolar ratio of 0.03 M.

SEM and XRD. The structural morphology of ZnO NWs was investigated by FESEM with a ZEISS Ultra+ microscope. A Bruker D8 Advance diffractometer using the Cu Kα1 radiation was employed in the Bragg−Brentano configuration in order to quantify the crystallinity and orientation of ZnO nanowires. The $\theta - 2\theta$ XRD measurements were performed between 20 and 70° in 2θ scale. X-ray pole figures were performed with a Siemens D5000 diffractometer using the Cu Kα1 radiation and equipped with a four-circle goniometer, 2.5° Sollers slits, a graphite monochromator, and a scintillation detector. The vertical alignment of ZnO nanostructures was determined by considering the fwhm of the (0002) diffraction peak. The homoepitaxial relationship of ZnO was further investigated by considering the (11$\bar{2}$2) asymmetric diffraction peak.

TEM and CBED. The structural morphology of ZnO NWs as well as the interface quality with polar c-plane ZnO single crystals was investigated by TEM imaging with a JEOL-JEM 2010 microscope operating at 200 kV with a 0.19 nm point-to-point resolution. All the specimens were prepared by focused ion beam (FIB) in a Zeiss NVision40 SEM-FIB microscope. The same microscope was used to perform CBED measurements in order to determine the polarity of ZnO NWs and c-plane ZnO single crystals by comparing relative orientations of experimental CBED patterns with associated TEM images of the crystal. The identification was based on the fact that the 0002 and 000$\bar{2}$ diffraction disks are significantly asymmetric in CBED patterns recorded along the $\langle 10\bar{1}0 \rangle$ zone axis. CBED patterns are distinctive of the material and strongly depend on the crystal thickness. The necessary simulations along the $\langle 10\bar{1}0 \rangle$ zone axis of ZnO using Bloch's wave method were performed with EMS software, checking always that the simulated diffraction spots are correctly labeled with respect to the simulated starting crystal structure.[69] A series of simulations was performed where the crystal thickness was varied from 20 to 300 nm with a 1 nm step. Moreover, any rotations produced in the microscope between the TEM images and CBED patterns were carefully considered for the polarity determination.

CL. The optical properties of ZnO NWs were determined by 5 K CL measurements with an Inspect F50 FEI FESEM equipped with a liquid-helium-cooled stage. The CL signal was collected *via* a parabolic mirror and analyzed with a 460 mm focal length monochromator equipped with 600 and 1800 grooves/mm diffraction gratings. The CL spectra were recorded with a nitrogen-cooled silicon CCD detector. The low acceleration voltage of 5 kV and small spot size (*i.e.*, less than 10 nm) were used to collect the CL signal at the center of single ZnO NWs.

Conflict of Interest: The authors declare no competing financial interest.

REFERENCES AND NOTES

1. Law, M.; Goldberger, J.; Yang, P. Semiconductor Nanowires and Nanotubes. *Annu. Rev. Mater. Res.* **2004**, *34*, 83–122.
2. Lieber, C. M.; Wang, Z. L. Functional Nanowires. *MRS Bull.* **2007**, *32*, 99–108.
3. Garnett, E. C.; Brongersma, M. L.; Cui, Y.; McGehee, M. D. Nanowire Solar Cells. *Annu. Rev. Mater. Res.* **2011**, *41*, 269–295.
4. Wang, Z. L. Zinc Oxide Nanostructures: Growth, Properties and Applications. *J. Phys.: Condens. Matter* **2004**, *16*, R829–R858.
5. Yi, G. C.; Wang, C.; Park, W. I. ZnO Nanorods: Synthesis, Characterization and Applications. *Semicond. Sci. Technol.* **2005**, *20*, S22–S34.
6. Pan, Z. W.; Dai, Z. R.; Wang, Z. L. Nanobelts of Semiconducting Oxides. *Science* **2001**, *291*, 1947–1949.
7. Lyu, S. C.; Zhang, Y.; Lee, C. J.; Ruh, H.; Lee, H. J. Low-Temperature Growth of ZnO Nanowire Array by a Simple Physical Vapor-Deposition Method. *Chem. Mater.* **2003**, *15*, 3294–3299.
8. Sun, Y.; Fuge, G. M.; Ashfold, M. N. R. Growth of Aligned ZnO Nanorod Arrays by Catalyst-Free Pulsed Laser Deposition Methods. *Chem. Phys. Lett.* **2004**, *396*, 21–26.
9. Wu, J. J.; Liu, S. C. Low-Temperature Growth of Well-Aligned ZnO Nanorods by Chemical Vapor Deposition. *Adv. Mater.* **2002**, *14*, 215–218.
10. Park, W. I.; Kim, D. H.; Jung, S. W.; Yi, G. C. Metal-Organic Vapor Phase Epitaxial Growth of Vertically Well-Aligned ZnO Nanorods. *Appl. Phys. Lett.* **2002**, *80*, 4232–4234.
11. Zheng, M. J.; Zhang, L. D.; Li, G. H.; Shen, W. Z. Fabrication and Optical Properties of Large-Scale Uniform Zinc Oxide Nanowire Arrays by One-Step Electrochemical Deposition Technique. *Chem. Phys. Lett.* **2002**, *363*, 123–128.
12. Vayssieres, L.; Keis, K.; Lindquist, S. E.; Hagfeldt, A. Purpose-Built Anisotropic Metal Oxide Material: 3D Highly Oriented Microrod Array of ZnO. *J. Phys. Chem. B* **2001**, *105*, 3350–3352.
13. Gonakowski, J.; Finocchi, F.; Noguera, C. Polarity of Oxide Surfaces and Nanostructures. *Rep. Prog. Phys.* **2008**, *71*, 016501.
14. Postels, B.; Kreye, M.; Wehmann, H. H.; Bakin, A.; Boukos, N.; Travlos, A.; Waag, A. Selective Growth of ZnO Nanorods in Aqueous Solution. *Superlattices Microstruct.* **2007**, *42*, 425–430.
15. Ahsanulhaq, Q.; Kim, J. H.; Hahn, Y. B. Controlled Selective Growth of ZnO Nanorod Arrays and Their Field Emission Properties. *Nanotechnology* **2007**, *18*, 485307.
16. Yan, X.; Li, Z.; Chen, R.; Gao, W. Template Growth of ZnO Nanorods and Microrods with Controllable Densities. *Cryst. Growth Des.* **2008**, *8*, 2406–2410.
17. Lee, S. H.; Minegishi, T.; Park, J. S.; Park, S. H.; Ha, J. S.; Lee, H. J.; Lee, H. J.; Ahn, S.; Kim, J.; Jeon, H.; *et al.* Ordered Arrays of ZnO Nanorods Grown on Periodically Polarity-Inverted Surfaces. *Nano Lett.* **2008**, *8*, 2419–2422.
18. Li, C.; Hong, G.; Wang, P.; Yu, D.; Qi, L. Wet Chemical Approaches to Patterned Arrays of Well-Aligned ZnO Nanopillars Assisted by Monolayer Colloidal Crystals. *Chem. Mater.* **2009**, *21*, 891–897.
19. Ahsanulhaq, Q.; Kim, J. H.; Hahn, Y. B. Density-Controlled Selective Growth of Well-Aligned ZnO Nanorod Arrays by a Hybrid Approach. *Superlattices Microstruct.* **2010**, *48*, 162–169.
20. Park, J.; Kim, K. H.; Park, S. H.; Yoon, E.; Yao, T. Catalyst-Free Growth of Vertically Aligned ZnO Nanostructures Arrays on Periodically Polarity-Inverted Substrate. *Appl. Phys. Express* **2010**, *3*, 105001.
21. Zhang, J.; Que, W.; Jia, Q.; Ye, X.; Ding, Y. Controllable Hydrothermal Synthesis of ZnO Nanowire Arrays on Al-Doped ZnO Seed Layer and Patterning of ZnO Nanowire Arrays *via* Surface Modification of Substrates. *Appl. Phys. Surf.* **2011**, *257*, 10134–10140.
22. Ahsanulhaq, Q.; Kim, J. H.; Hahn, Y. B. Etch-Free Selective Area Growth of Well-Aligned ZnO Nanorod Arrays by Economical Polymer Mask for Large-Area Solar Cell Applications. *Sol. Energy Mater. Sol. Cells* **2012**, *98*, 476–481.
23. Park, J.; Yao, T. Position-Controlled Vertical Arrays of Single-Crystalline ZnO Nanowires on Periodically Polarity Inverted Templates. *J. Alloys Compd.* **2012**, *513*, 180–183.
24. Park, H. H.; Zhang, X.; Lee, K. W.; Kim, K. H.; Jung, S. H.; Park, D. S.; Choi, Y. S.; Shin, H. B.; Sung, H. K.; Park, K. H.; *et al.* Position-Controlled Hydrothermal Growth of ZnO Nanorods on Arbitrary Substrates with a Patterned Seed Layer *via* Ultra-violet Assisted Nanoimprint Lithography. *CrystEngComm* **2013**, *15*, 3463–3469.
25. Wang, X.; Summers, J.; Wang, Z. L. Large-Scale Hexagonal-Patterned Growth of Aligned ZnO Nanorods for Nano-optoelectronics and Nanosensor Arrays. *Nano Lett.* **2004**, *4*, 423–426.

26. Kim, Y. J.; Lee, C. H.; Hong, Y. J.; Yi, G. C.; Kim, S. S.; Cheong, H. Controlled Selective Growth of ZnO Nanorod and Microrod Arrays on Si Substrates by a Wet Chemical Method. *Appl. Phys. Lett.* **2006**, *89*, 163128.

27. Weintraub, B.; Deng, Y.; Wang, Z. L. Position-Controlled Seedless Growth of ZnO Nanorod Arrays on a Polymer Substrate *via* Wet Chemical Synthesis. *J. Phys. Chem. C* **2007**, *111*, 10162–10165.

28. Cui, J.; Gibson, U. Low-Temperature Fabrication of Single-Crystal ZnO Nanopillar Photonic Bandgap Structures. *Nanotechnology* **2007**, *18*, 155302.

29. Xu, S.; Wei, Y.; Kirkham, M.; Liu, J.; Mai, W.; Davidovic, D.; Snyder, R. L.; Wang, Z. L. Patterned Growth of Vertically Aligned ZnO Nanowire Arrays on Inorganic Substrates at Low Temperature without Catalyst. *J. Am. Chem. Soc.* **2008**, *130*, 14958–14959.

30. Zhang, S.; Shen, Y.; Fang, H.; Xu, S.; Song, J.; Wang, Z. L. Growth and Replication of Ordered ZnO Nanowire Arrays on General Flexible Substrates. *J. Mater. Chem.* **2010**, *20*, 10606–10610.

31. Wei, Y.; Wu, W.; Guo, R.; Yuan, D.; Das, S.; Wang, Z. L. Wafer-Scale High-Throughput Ordered Growth of Vertically Aligned ZnO Nanowire Arrays. *Nano Lett.* **2010**, *10*, 3414–3419.

32. Li, G. P.; Jiang, L.; Wang, S. J.; Sun, X. W.; Chen, X.; Wu, T. Buffer-Layer-Assisted Epitaxial Growth of Perfectly Aligned Oxide Nanorod Arrays in Solution. *Cryst. Growth Des.* **2011**, *11*, 4885–4891.

33. Richardson, J. J.; Estrada, D.; DenBaars, S. P.; Hawker, C. J.; Campos, L. M. A Facile Route to Patterned Epitaxial ZnO Nanostructures by Soft Lithography. *J. Mater. Chem.* **2011**, *21*, 14417–14419.

34. Oh, S.; Nagata, T.; Volk, J.; Wakayama, Y. Nanoimprint for Fabrication of Highly Ordered Epitaxial ZnO Nanorods on Transparent Conductive Oxide Films. *Appl. Phys. Express* **2012**, *5*, 095003.

35. He, Y.; Yanagida, T.; Nagashima, K.; Zhuge, F.; Meng, G.; Xu, B.; Klamchuen, A.; Rahong, S.; Kanai, M.; Li, X.; *et al.* Crystal-Plane Dependence of Critical Concentration for Nucleation on Hydrothermal ZnO Nanowires. *J. Phys. Chem. C* **2013**, *117*, 1197–1203.

36. Hong, Y. J.; An, S. J.; Jung, H. S.; Lee, C. H.; Yi, G. C. Position-Controlled Selective Growth of ZnO Nanorods on Si Substrates Using Facet-Controlled GaN Micropatterns. *Adv. Mater.* **2007**, *19*, 4416–4419.

37. Wang, Z. L.; Kong, X. Y.; Zuo, J. M. Induced Growth of Asymmetric Nanocantilever Arrays on Polar Surfaces. *Phys. Rev. Lett.* **2003**, *91*, 185502.

38. Baxter, J. B.; Wu, F.; Aydil, E. S. Growth Mechanism and Characterization of Zinc Oxide Hexagonal Columns. *Appl. Phys. Lett.* **2003**, *83*, 3797–3799.

39. Scrymgeour, D. A.; Sounart, T. L.; Simmons, N. C.; Hsu, J. W. P. Polarity and Piezoelectric Response of Solution Grown Zinc Oxide Nanocrystals on Silver. *J. Appl. Phys.* **2007**, *101*, 014316.

40. Nicholls, D. P.; Vincent, R.; Cherns, D.; Sun, Y.; Ashfold, M. N. R. Polarity Determination of Zinc Oxide Nanorods by Defocused Convergent-Beam Electron Diffraction. *Philos. Mag. Lett.* **2007**, *87*, 417–421.

41. Cherns, D.; Sun, Y. Defect Reduction by Epitaxial Lateral Overgrowth of Nanorods in ZnO/(0001) Sapphire Films. *Appl. Phys. Lett.* **2008**, *92*, 051909.

42. Sun, Y.; Cherns, D.; Doherty, R. P.; Warren, J. L.; Heard, P. J. Reduction of Threading Dislocations in ZnO/(0001) Sapphire Film Heterostructure by Epitaxial Lateral Overgrowth of Nanorods. *J. Appl. Phys.* **2008**, *104*, 023533.

43. Song, T.; Choung, J. W.; Park, J.-G.; Park, W. I.; Rogers, J. A.; Paik, U. Surface Polarity and Shape-Controlled Synthesis of ZnO Nanostructures on GaN Thin Films Based on Catalyst-Free Metalorganic Vapor Phase Epitaxy. *Adv. Mater.* **2008**, *20*, 4464–4469.

44. Perillat-Merceroz, G.; Jouneau, P. H.; Feuillet, G.; Thierry, R.; Rosina, M.; Ferret, P. MOCVD Growth Mechanisms of ZnO Nanorods. *J. Phys. Conf. Ser.* **2010**, *209*, 012034.

45. Perillat-Merceroz, G.; Thierry, R.; Jouneau, P.H.; Ferret, P.; Feuillet, G. Compared Growth Mechanisms of Zn-Polar ZnO Nanowires on O-Polar ZnO and on Sapphire. *Nanotechnology* **2012**, *23*, 125702.

46. Lee, W. W.; Kim, S. B.; Yi, J.; Nichols, W. T.; Park, W. I. Surface Polarity-Dependent Cathodoluminescence in Hydrothermally Grown ZnO Hexagonal Rods. *J. Phys. Chem. C* **2012**, *116*, 456–460.

47. Guillemin, S.; Rapenne, L.; Roussel, H.; Sarigiannidou, E.; Brémond, G.; Consonni, V. Formation Mechanisms of ZnO Nanowires: The Crucial Role of Crystal Orientation and Polarity. *J. Phys. Chem. C* **2013**, *117*, 20738–20745.

48. Käbisch, S.; Gluba, M. A.; Klimm, C.; Krause, S.; Koch, N.; Nickel, N. H. Polarity-Driven Morphology of Zinc Oxide Nanostructures. *Appl. Phys. Lett.* **2013**, *103*, 103106.

49. Sallet, V.; Sartel, C.; Vilar, C.; Lusson, A.; Galtier, P. Opposite Crystal Polarities Observed in Spontaneous and Vapor–Liquid–Solid Grown ZnO Nanowires. *Appl. Phys. Lett.* **2013**, *102*, 182103.

50. De la Mata, M.; Magen, C.; Gazquez, J.; Iqbal Bakti Utama, M.; Heiss, M.; Lopatin, S.; Furtmayr, F.; Fernández-Rojas, C. J.; Peng, B.; Morante, J. R.; *et al.* Polarity Assignment in ZnTe, GaAs, ZnO, and GaN-AlN Nanowires from Direct Dumbbell Analysis. *Nano Lett.* **2012**, *12*, 2579–2586.

51. Yamabi, S.; Imai, H. Growth Conditions for Wurtzite Zinc Oxide Films in Aqueous Solutions. *J. Mater. Chem.* **2002**, *12*, 3773–3778.

52. Greene, L. E.; Law, M.; Goldberger, J.; Kim, F.; Johnson, J. C.; Zhang, Y.; Saykally, R. J.; Yang, P. Low-Temperature Wafer-Scale Production of ZnO Nanowire Arrays. *Angew. Chem., Int. Ed.* **2003**, *42*, 3031–3034.

53. Choy, J. H.; Jang, E. S.; Won, J. H.; Chung, J. H.; Jang, D. J.; Kim, Y. W. Soft Solution Route to Directionally Grown ZnO Nanorod Arrays on Si Wafer; Room-Temperature Ultraviolet Laser. *Adv. Mater.* **2003**, *15*, 1911–1914.

54. Hung, C. H.; Whang, W. T. A. A Novel Low-Temperature Growth and Characterization of Single Crystal ZnO Nanorods. *Mater. Chem. Phys.* **2003**, *82*, 705–710.

55. Chen, S. W.; Wu, J. M. Nucleation Mechanisms and their Influences on Characteristics of ZnO Nanorod Arrays Prepared by a Hydrothermal Method. *Acta Mater.* **2011**, *59*, 841–847.

56. Guillemin, S.; Consonni, V.; Appert, E.; Puyoo, E.; Rapenne, L.; Roussel, H. Critical Nucleation Effects on the Structural Relationship between ZnO Seed Layer and Nanowires. *J. Phys. Chem. C* **2012**, *116*, 25106–25111.

57. Consonni, V.; Rey, G.; Bonaime, J.; Karst, N.; Doisneau, B.; Roussel, H.; Renet, S.; Bellet, D. Synthesis and Physical Properties of ZnO/CdTe Core Shell Nanowires Grown by Low-Cost Deposition Methods. *Appl. Phys. Lett.* **2011**, *98*, 111906.

58. Sun, Y.; Riley, D. J.; Ashfold, M. N. R. Mechanism of ZnO Nanotube Growth by Hydrothermal Methods on ZnO Film-Coated Si Substrates. *J. Phys. Chem. B* **2006**, *110*, 15186–15192.

59. Ashfold, M. N. R.; Doherty, R. P.; Ndifor-Angwafor, N. G.; Riley, D. J.; Sun, Y. The Kinetics of the Hydrothermal Growth of ZnO Nanostructures. *Thin Solid Films* **2007**, *515*, 8579–8683.

60. McPeak, K. M.; Becker, M. A.; Britton, N. G.; Majidi, H.; Bunker, B. A.; Baxter, J. B. *In Situ* X-ray Absorption Near-Edge Structure Spectroscopy of ZnO Nanowire Growth during Chemical Bath Deposition. *Chem. Mater.* **2010**, *22*, 6162–6170.

61. McPeak, K. M.; Le, T. P.; Britton, N. G.; Nickolov, Z. S.; Elabd, Y. A.; Baxter, J. B. Chemical Bath Deposition of ZnO Nanowires at Near-Neutral pH Conditions without Hexamethylenetetramine (HMTA): Understanding the Role of HMTA in ZnO Nanowire Growth. *Langmuir* **2011**, *27*, 3672–3677.

62. Govender, K.; Boyle, D. S.; Kenway, P. B.; O'Brien, P. Understanding the Factors That Govern the Deposition and Morphology of Thin Films of ZnO from Aqueous Solution. *J. Mater. Chem.* **2004**, *14*, 2575–2591.

63. Boercker, J. E.; Schmidt, J. B.; Aydil, E. S. Transport Limited Growth of Zinc Oxide Nanowires. *Cryst. Growth Des.* **2009**, *9*, 2783–2789.

64. Woell, C. The Chemistry and Physics of Zinc Oxide Surfaces. *Prog. Surf. Sci.* **2007**, *82*, 55–120.

65. Sugunan, A.; Warad, H. C.; Boman, M.; Dutta, J. Zinc Oxide Nanowires in Chemical Bath on Seeded Substrates: Role of Hexamine. *J. Sol−Gel Sci. Technol.* **2006**, *39*, 49–56.

66. Liliental-Weber, Z.; Kisielowski, C. H.; Rumivov, S.; Chen, Y.; Washburn, J.; Grzegory, I.; Bockowski, M.; Jun, J.; Porowski, S. Structural Characterization of Bulk GaN Crystals Grown under High Hydrostatic Pressure. *J. Electron. Mater.* **1996**, *25*, 1545–1550.

67. Ponce, F. A.; Bour, D. P.; Young, W. T.; Saunders, M.; Steeds, J. W. Determination of Lattice Polarity for Growth of GaN Bulk Single Crystals and Epitaxial Layers. *Appl. Phys. Lett.* **1996**, *69*, 337–339.

68. Daudin, B.; Rouvière, J. L.; Arlery, M. Polarity Determination of GaN Films by Ion Channeling and Convergent Beam Electron Diffraction. *Appl. Phys. Lett.* **1996**, *69*, 2480–2482.

69. Stadelmann, P. A. EMS: A Software Package for Electron Diffraction Analysis and HREM Image Simulation in Materials Science. *Ultramicroscopy* **1987**, *21*, 131.

70. Chen, X. J.; Perillat-Merceroz, G.; Sam-Jiao, D.; Durand, C.; Eymery, J. Homoepitaxial Growth of Catalyst-Free GaN Wires on N-Polar Substrates. *Appl. Phys. Lett.* **2010**, *97*, 151909.

71. Fernandez-Garrido, S.; Kong, X.; Gotschke, T.; Calarco, R.; Geelhaar, L.; Trampert, A.; Brandt, O. Spontaneous Nucleation and Growth of GaN Nanowires: The Fundamental Role of Crystal Polarity. *Nano Lett.* **2012**, *12*, 6119–6125.

72. Meyer, B. K.; Alves, H.; Hofmann, D. M.; Kriegseis, W.; Forster, D.; Bertram, F.; Christen, J.; Hoffmann, A.; Strassburg, M.; Dworzak, M.; *et al.* Bound Exciton and Donor−Acceptor Pair Recombinations in ZnO. *Phys. Status Solidi B* **2004**, *241*, 231–260.

73. Meyer, B.; Sann, J.; Lautenschläger, S.; Wagner, M. R.; Hoffmann, A. Ionized and Neutral Donor-Bound Excitons in ZnO. *Phys. Rev. B* **2007**, *76*, 184120.

74. Dong, Y.; Fang, Z. Q.; Look, D. C.; Cantwell, G.; Zhang, J.; Song, J. J.; Brillson, L. J. Zn- and O-Face Polarity Effects at ZnO Surfaces and Metal Interfaces. *Appl. Phys. Lett.* **2008**, *93*, 072111.

75. Lautenschlaeger, S.; Sann, J.; Volbers, N.; Meyer, B. K.; Hoffmann, A.; Haboeck, U.; Wagner, M. R. Asymmetry in the Excitonic Recombinations and Impurity Incorporation of the Two Polar Faces of Homoepitaxially Grown ZnO Films. *Phys. Rev. B* **2008**, *77*, 144108.

76. Wang, Z. L.; Song, J. H. Piezoelectric Nanogenerators Based on Zinc Oxide Nanowire Arrays. *Science* **2006**, *312*, 242–246.

77. Puyoo, E.; Rey, G.; Appert, E.; Consonni, V.; Bellet, D. Efficient Dye-Sensitized Solar Cells Made from ZnO Nanostructure Composites. *J. Phys. Chem. C* **2012**, *116*, 18117–18123.

78. Levy-Clement, C.; Tena-Zaera, R.; Ryan, M. A.; Katty, A.; Hodes, G. CdSe-Sensitized p-CuSCN/Nanowire n-ZnO Heterojunctions. *Adv. Mater.* **2005**, *17*, 1512–1515.

79. Wu, Z.; Zhang, Y.; Zheng, J.; Lin, X.; Chen, X.; Wang, B.; Wang, H.; Huang, K.; Li, S.; Kang, J. An All-Inorganic Type II Heterojunction Array with Nearly Full Solar Spectral Response Based on ZnO/ZnSe Core/Shell Nanowires. *J. Mater. Chem.* **2011**, *21*, 6020–6026.